Research Article | Vol. 30, No. 10 / 9 May 2022 / Optics Express 15998

Optics EXPRESS

Polarimetric fiber laser for relative humidity sensing based on graphene oxide-coated D-shaped fiber and beat frequency demodulation

KUIKUI GUO,[1,2] JUN HE,[1,2,*] HE LI,[1,2] XIZHEN XU,[1,2] BIN DU,[1,2] SHEN LIU,[1,2] YANPING CHEN,[1,2] DINGBANG MA,[1,2] YING WANG,[1,2] GAIXIA XU,[3] AND YIPING WANG[1,2]

[1] *Key Laboratory of Optoelectronic Devices and Systems of Ministry of Education/Guangdong Province, College of Physics and Optoelectronic Engineering, Shenzhen University, Shenzhen 518060, China*
[2] *Shenzhen Key Laboratory of Photonic Devices and Sensing Systems for Internet of Things, Guangdong and Hong Kong Joint Research Centre for Optical Fibre Sensors, Shenzhen University, Shenzhen 518060, China*
[3] *Guangdong Key Laboratory for Biomedical Measurements and Ultrasound Imaging, School of Biomedical Engineering, Shenzhen University Health Science Center, Shenzhen 518060, China*
[*] *hejun07@szu.edu.cn*

Abstract: We first propose and demonstrate a polarimetric fiber laser system for relative humidity (RH) sensing based on the beat frequency demodulation. A graphene oxide-coated D-shaped fiber (GDF) with a low insertion loss of 0.8 dB was embedded into a laser cavity to form an RH sensing probe. The output of the fiber laser could generate mode splitting between two orthogonal polarization modes due to birefringence of the GDF device. Hence, two types of beat signals, i.e., longitudinal mode beat frequency (LMBF) and polarization mode beat frequency (PMBF) could be generated synchronously. The experimental results indicated that the LMBFs of the fiber laser had almost no response to the ambient humidity, and the PMBFs of the fiber laser were very sensitive to the various RH levels. There was a good linear relationship between the PMBF and RH changes in the range of 30% to 98%. This fiber-optic RH sensor exhibited a sensitivity of 34.7 kHz/RH% with a high quality of fit (R^2>0.997) during the ambient RH increase and decrease. Moreover, the average response and recovery times of the fiber-optic RH sensor were measured to be about 64.2 ms and 97.8 ms, respectively. Due to its long stability, reversibility, quick response time and low temperature cross-sensitivity (i.e., 0.12 RH%/°C), the proposed fiber-optic RH sensor could offer attractive applications in many fields, such as biology, chemical processing and food processing, etc.

1. Introduction

Relative humidity (RH) sensors play an important role in food processing, agriculture, biology, structural health monitoring, instrument manufacturing, and many other fields [1].Compared to traditional electrical RH sensors, fiber-optic RH sensors have the advantages of low costs, anti-electromagnetic interference, anti-corrosion, and remote detection capacity [2]. Recently, massive RH sensors based on optical fiber devices have been proposed, such as fiber Bragg gratings (FBGs) [3,4], tilted fiber Bragg gratings (TFBGs) [5], long period gratings (LPGs) [6], and many kinds of fiber-optic interferometers [7–13]. In particular, some fiber-optic RH sensors consist of the microfiber [14], hollow core fiber [15], no-core fiber [16], plastic optical fiber [17], few-mode fiber [18,19], polarization-maintaining fiber (PMF) [8], side-polished fiber [20], and photonic crystal fiber (PCF) [21]. However, these fiber-optic RH sensors listed above have a few defects: (1) the manufacture of fiber gratings, fiber-optic interferometers and microfiber structures is complicated. (2) The costs of some special fiber (e.g., PMF and PCF) are very high.

#457297 https://doi.org/10.1364/OE.457297
Journal © 2022 Received 28 Feb 2022; revised 12 Apr 2022; accepted 16 Apr 2022; published 25 Apr 2022

(3) The insertion loss of some fiber-optic RH sensors is very large. Considering all the factors described above, the side-polished fiber, i.e., D-shaped fiber with a low insertion loss is more suitable for an RH sensor due to its low cost and simple fabrication process. Moreover, various humidity-sensitive polyimide [3], chitosan [22], metal oxides [23], polymethyl methacrylate [24], agarose gel [25], polyvinyl alcohol [26], and tungsten disulfide [27] are always required to coat the surfaces of fiber devices to enhance the sensitivity of RH sensors. However, in these studies, the refractive index change of the coated material was closely related to the penetration capacity of the water molecules, and the poor penetrability of the water molecules may lead to the hysteresis. Additionally, many efforts have been devoted to fabricate high-performance fiber-optic gas sensors based on 2D material graphene [28–31]. However, these fiber-optic sensors exhibited slow response time or small measurement range. To address this issue, the graphene oxide (GO) can be considered an outstanding candidate for high sensitivity RH sensing due to its large specific surface area and massive functional groups including hydroxyl, carboxyl and carbonyl [32,33], which could lead to fast response time and large measurement range of optic-fiber RH sensors.

The fiber-optic RH sensors discussed above are mainly classified into two categories, i.e., wavelength-encoded sensors and intensity-encoded sensors. The former ones convert the measurand into the wavelength variation of the spectral peak or notch location, and these sensors typically suffer from a low response rate due to the mechanical wavelength scanning process. The latter ones rely on the detection of optical power change with the different RH levels, and these sensors are easily affected by optical power fluctuations. Fortunately, the beat frequency demodulation method has garnered great interest in recent years [34,35] and opened a new avenue for fiber laser sensors due to its fast response rate. A weak change of the intracavity birefringence can obviously induce a polarization mode beat frequency (PMBF) shift. The measurand can be converted into a corresponding change in the PMBF of the fiber laser. Hence, massive polarimetric fiber laser sensors for measuring the hydrostatic pressure, lateral force, temperature, strain and ultrasound based on a beat frequency demodulation have been reported [34–37]. In 2021, Yao *et al.* realized a two-dimensional-material functionalized microcomb gas sensor by depositing graphene in an over-modal microsphere, which can offer high sensitivity for the detection of gas mixtures without cross-sensitivity issues based on a beat frequency demodulation [38]. Compared to the two kinds of fiber-optic RH sensors described above, a polarimetric fiber laser sensor only need a photo-detector and a frequency spectrum analyzer to interrogate the beat signals, which means that this type of fiber laser possesses several advantages of a simple structure, decrease in complexity, and immunity to intensity perturbation.

In this research, we proposed a fiber laser system for RH sensing based on the beat frequency demodulation. The RH sensor probe was formed by a graphene oxide-coated D-shaped fiber. This proposed fiber-optic RH sensor exhibited a high sensitivity of 34.7 kHz/RH% during the increase and decrease of the ambient RH. Additionally, the average response and recovery times of the fiber-optic RH sensor were measured to be about 64.2 ms and 97.8 ms, respectively. The experimental results indicated that the proposed fiber-optic RH sensor had the advantages of long stability, reversibility, a quick response, and a low temperature cross-sensitivity.

2. Sensing mechanism

Figure 1 shows a schematic diagram of the polarimetric fiber laser based on graphene oxide-coated D-shaped fiber (GDF). The fiber laser consisted of an FBG, a section of erbium-doped fiber (EDF, Nufern SM-ESF-7/125, peak absorption: 55 dB/m @ 1530 nm), and a loop mirror to form the laser cavity. The FBG and the coupler could play a role in the two reflectors, and the EDF acted as the gain medium. The pump light from a 980 nm laser diode was transmitted through a 980 nm optical isolator (ISO) and a wavelength division multiplexer (WDM). Then the pump light was injected into the laser cavity. The function of the ISO is to suppress the reflected 980 nm pump laser. According to the laser principle, many longitudinal modes were excited in the long laser cavity when the pump threshold condition was satisfied. When the GDF was inserted into the laser cavity, the orthogonal polarization modes (i.e., ν_x and ν_y) were not degenerate due to the birefringence effect in GDF. As a result, the slight mode splitting phenomenon (i.e., $\nu'_x \neq \nu'_y$) occurred. The birefringence value of the GDF could be defined as:

$$B = |n_x - n_y|, \tag{1}$$

where n_x and n_y are the refractive indices of the slow and fast axes. Hence, there exists two types of beat frequency signals, i.e., the longitudinal mode beat frequency (LMBF) and polarization mode beat frequency (PMBF). It is noted that the generation mechanism of the LMBF and PMBF are different. The LMBF are induced by two different longitudinal modes at x or y direction. The PMBF are caused by two different polarization modes [39].

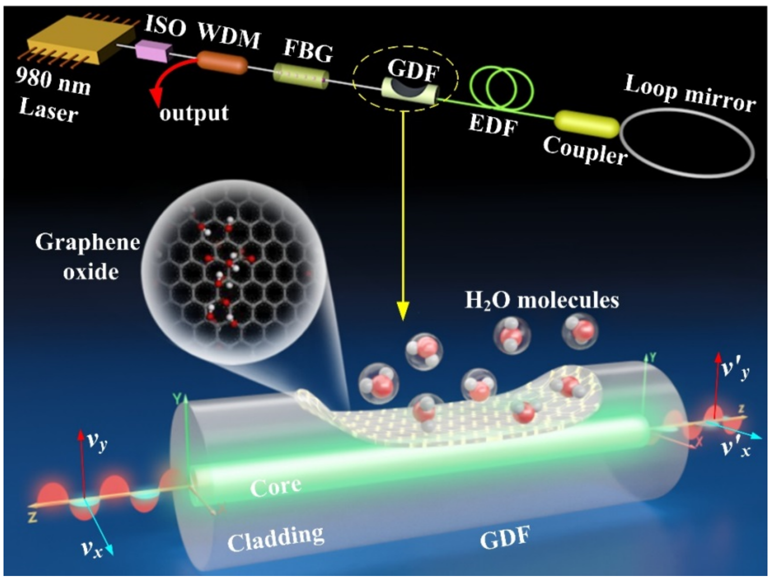

Fig. 1. Schematic diagram of the polarimetric fiber laser based on a graphene oxide-coated D-shaped fiber (GDF). ISO: isolator; WDM: wavelength division multiplexer; FBG: fiber Bragg grating; EDF: erbium-doped fiber.

For the multi-longitudinal mode fiber laser, the j-order longitudinal mode of fiber laser could be expressed as [40]:

$$f_j = \frac{jc}{2nL}, \tag{2}$$

where j is the number of the longitudinal mode, c is the light speed in empty space, n is the effective refractive index of the fiber, and L is the total laser cavity length. The LMBF of the fiber laser could be written as [35]:

$$f_N = (j-i)\frac{c}{2nL} = \frac{Nc}{2nL}, \tag{3}$$

where i is the number of the longitudinal mode, and $N = j\text{-}i$ ($N = 1, 2, 3\ldots$). Due to the fiber intrinsic birefringence, the frequency values of the two orthogonal polarization modes were different. As a result, the PMBF induced by the birefringence effect could be written as:

$$f_B = f_x - f_y = \frac{(n_x - n_y)jc}{2n_x n_y L} = \frac{B}{n} f_j, \tag{4}$$

where n_x and n_y are the effective refractive indices of the two orthogonal polarization modes. If the polarization mode beat signals caused by other laser modes with different polarization directions are considered, a general expression for describing the PMBFs can be written as:

$$f_p = \{f_B, f_N \pm f_B\} = \left\{\frac{B}{n} f_j, \frac{Nc}{2nL} \pm \frac{B}{n} f_j\right\}. \tag{5}$$

When different RH was applied to the GDF, the refractive index of the graphene oxide could be obviously changed due to its excellent hydrophilicity. Hence, the birefringence of the GDF could be also changed, resulting in the PMBF shift. The sensitivity between the PMBFs and the RH could be expressed as:

$$S = \frac{df_p}{dRH} = \left\{\frac{f_j}{n}\frac{dB}{dRH}, \frac{Nc}{2nL} \pm \frac{f_j}{n}\frac{dB}{dRH}\right\}. \tag{6}$$

From Eq. (6), the sensitivity was mainly determined by the RH-induced birefringence variation dB/dRH.

3. Device fabrication

3.1. Fabrication procedure

Figure 2 demonstrates the fabrication process for the proposed GDF device. In step 1, the D-shaped fiber (DF) was fabricated using a high precision wheel polishing setup (WanRun Ltd., WuXi, China), as shown in Fig. 2(a). This fiber side-polishing method was similar to that of our previous study [41]. A 62 mm grinding wheel lined with an abrasive paper was translated across the singe-mode fiber (SMF, Corning) in the fiber axis direction. The SMF was gradually polished by a back-and-forth motion of the rolling wheel along the fiber. The lengths of the flat region and the tapered transition region were 10 and 2 mm. In step 2, the GO solution (XFNANO, Nanjing) was transferred onto the polishing surface of the DF via a pipette, as shown in Fig. 2(b). The DF was sequentially immersed into a series of GO solutions that could be synthesized with the Hummers method. The particle diameter and the concentration of the GO are about 50-200 nm and 2 mg/ml. In step 3, the DF coated with GO solution was dried using a heater, as shown in Fig. 2(c). The processes of step 2 and step 3 should be repeated many times to guarantee that the GO was evenly coated on the polishing surface of the DF. As shown in the inset of Fig. 2(c), the remaining thickness of the DF was defined as d, and the thickness of the GO film was defined as h.

3.2. Characterization of the RH sensor

When a 633 nm light was guided through the GDF, a strong scattering could be clearly seen on the GO-coated area due to the enhanced evanescent field, as shown in Fig. 3(a). Figure 3(b) illustrates the micrograph image of the GDF. The GO was evenly coated on the polishing surface of the DF. The cross-sectional scanning electron micrograph (SEM) of the GDF is shown in Fig. 3(c). The thickness h of the GO film was measured to be ~300 nm. Figure 3(d) illustrates the Raman spectrum of the GO film coated on the DF surface via a 532 nm laser excitation. It was clear that the characteristic peaks are located at 1340 cm^{-1} and 1600 cm^{-1}, corresponding to the D band and the G band, respectively. The D band corresponded to the respiratory vibration mode of a benzene ring atom, and its peak intensity characterized the disorder degree of the GO material. The G band corresponded to the mutual stretching mode of an SP^2 atom pair, and its

Optics EXPRESS

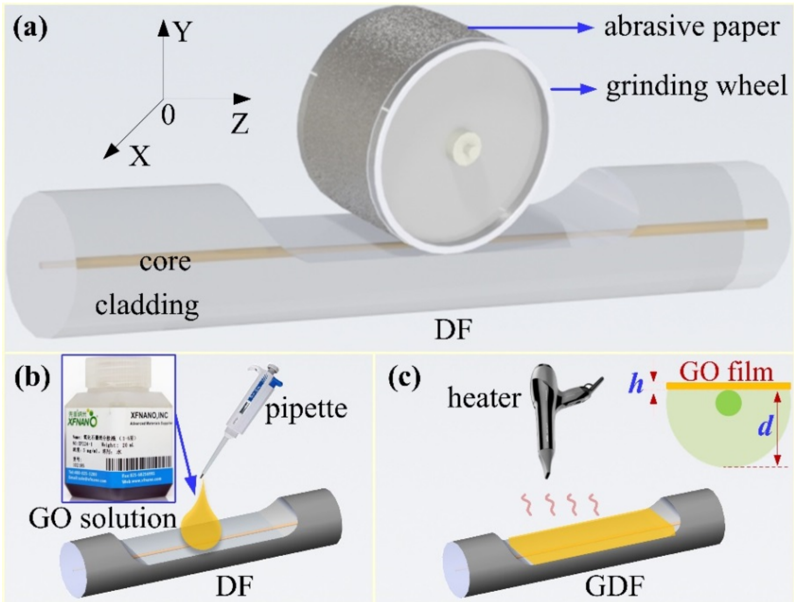

Fig. 2. Schematic diagrams of the fabrication process of the GDF humidity sensor.

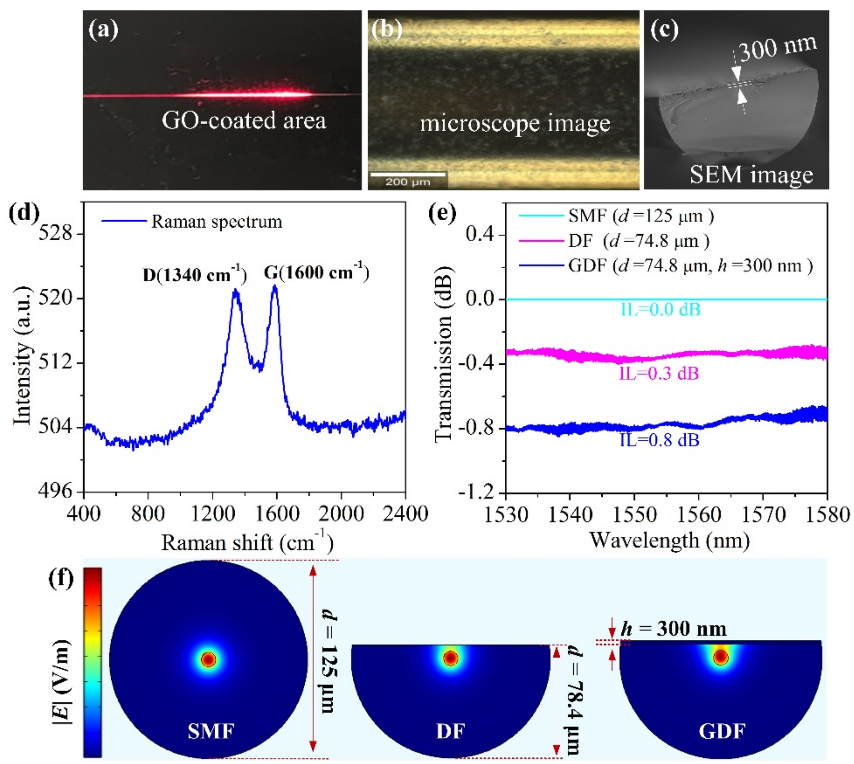

Fig. 3. (a) Strong scattering on the GO-coated area. (b) Micrograph image and (c) Cross-sectional SEM of the GDF. (d) Raman spectrum of the GO. (e) The transmission spectra of the SMF, DF and GDF. (f) Simulated mode distributions of the SMF, DF and GDF.

peak intensity indicated the number of SP^2 structure in the material. The features above indicated that the GO was effectively and tightly coated on the DF surface.

During the fabrication process of the GDF device, the transmission spectra of the SMF, DF, and GDF were measured online, as shown in Fig. 3(e). Compared to the SMF, the insertion loss (IL) of the DF could be increased to 0.3 dB with a remaining fiber thickness d of 74.8 µm. Finally, the total IL could be further increased to 0.8 dB when the GO was coated on the DF surface. In order to determine the effect that the GO film had on the transmission properties of the GDF device, the mode distributions of the SMF, the DF, and the GDF were simulated via a finite element method (FEM, COMSOL), as shown in Fig. 3(f). The remaining fiber thickness of the DF and the thickness of the GO film were set to 74.8 µm and 300 nm, respectively. It was clear that the evanescent field appeared the DF surface and the mode center of the GDF could be dragged closer to the GO film to further enhance the light-matter interaction.

4. Experiment and discussion

4.1. Experimental setup

Figure 4 illustrates the experimental setup of the polarimetric fiber laser for RH measurement. The output of the fiber laser was divided into two branches. One branch was detected by an optical spectrum analyzer (OSA, Yokagawa AQ6370C) with a resolution of 0.02 nm. The other branch was launched into a high speed photodetector (PD, Newfocus 1592) and then detected by a frequency spectrum analyzer (FSA, Rohde & Schwarz). The RH sensor (i.e., GDF device) was mounted and fixed in the gas chamber to prevent adverse bending and vibration. In this system, we used dry nitrogen as the carrier gas, and the humid gas could be produced to increase the humidity after the nitrogen passed through the water. Then, the RH value in the gas chamber could be precisely controlled from 30% to 98% by altering the flow rates of both the dry and humid gases. A commercial hygrometer (Rotronic, HygroPalm HP22) and) was placed in the gas chamber to monitor the RH variation online.

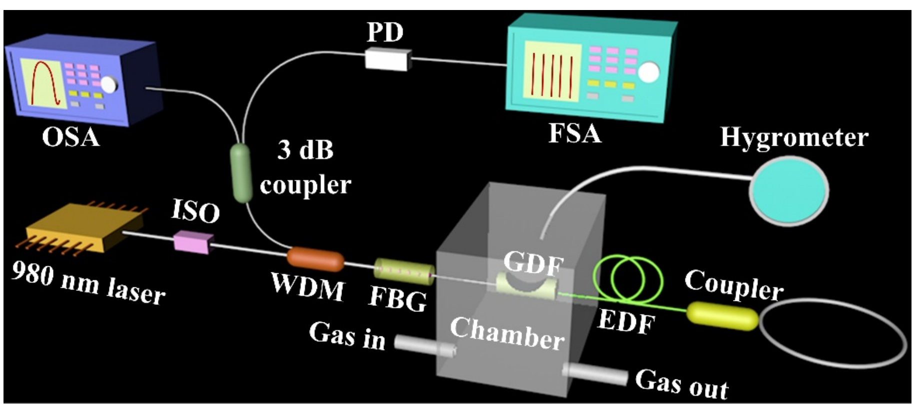

Fig. 4. The experimental setup of the polarimetric fiber laser for RH measurement.

4.2. Characterization of the polarimetric fiber laser

Figure 5(a) illustrates the optical spectrum of the grating (i.e., FBG) and the lasing spectrum of the polarimetric fiber laser. The FBG exhibited a transmission loss of -12.6 dB at a resonance wavelength of 1551.0 nm. It was obvious that the resonance wavelength of the grating could match the lasing wavelength of the fiber laser. Moreover, the output of the fiber laser exhibits a high signal-to-noise ratio (SNR) of 63.3 dB at a pump power of 30 mW. The beat frequency spectrum of the fiber laser was measured by an FSV with a resolution bandwidth of 10 kHz, as plotted in Fig. 5(b). The experimental results showed that several dominant beat signals, i.e., the LMBF f_N ($N = 1, 2, 3\ldots$) located at those positions of which have an equal frequency separation of 15.7 MHz, corresponding to a laser cavity length of ~ 6.6 m from Eq. (3) above. Additionally, two PMBFs (i.e., $f_N \pm f_B$) were located at both sides of the LMBF, and the SNRs of the dominant LMBF were obviously greater than those of the PMBF. The birefringence-induced beat frequency f_B had a small value of 3.4 MHz, corresponding to a fiber birefringence of ~ $2.6{*}10^{-8}$ from Eq. (4) above.

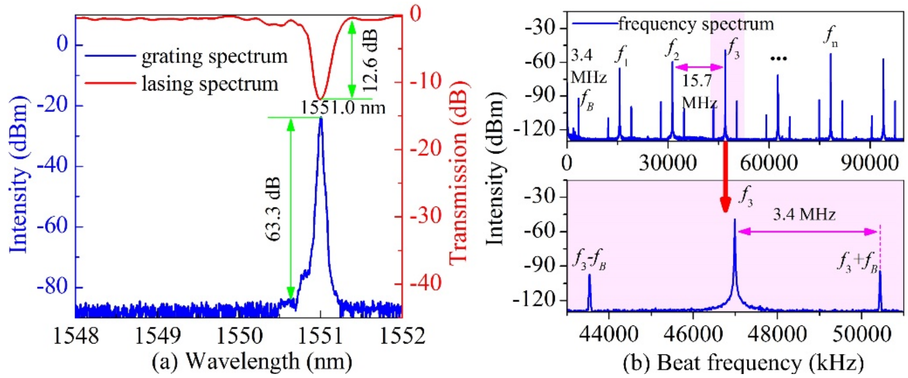

Fig. 5. (a) The optical spectrum of the grating (i.e., FBG) and the lasing spectrum of the fiber laser. (b) The beat frequency spectrum of the fiber laser.

4.3. Relative humidity response of the fiber-optic RH sensor

Figure 6(a) shows the beat signals of the polarimetric fiber laser at different RH levels. The beat frequency f_B shifted to a high frequency when the RH in the gas chamber was increased from 30% to 98% with a step size of 10% at room temperature. From Eq. (4), the birefringence of the GDF could be gradually increased with the RH increase. As a result, the PMBF (i.e., f_N-f_B, $N = 1, 2, 3\ldots$) on the left of the dominant LMBF shifted to a low frequency. Moreover, the LMBF f_N remained mostly unchanged with the RH increase. From Eq. (3) above, this meant that the different RH levels had no effect on the length of the fiber laser cavity. The LMBF at f_3 and PMBF at f_3-f_B were chosen as the monitored beat frequency signals for measuring the different RH values due to their relatively high SNR. As shown in Fig. 6(b), the PMBF at f_3-f_B shifted linearly with the RH increase and decrease. The RH sensitivity of -34.7 kHz/RH% with a high quality of fit (R^2>0.997) was obtained, which was higher than most of the fiber-optic RH sensors based on the GO material, as shown in Table 1 bellow. It was clear that the GDF device had high repeatability with no hysteresis phenomenon during the RH cycling. However, the LMBF at f_3 exhibited an extremely low RH sensitivity of -0.001 kH/RH%, which was consistent with the theoretical analysis described above.

4.4. Stability and response time of the fiber-optic RH sensor

The stability was an important parameter of the fiber-optic RH sensor. As shown in Fig. 7(a), the BMBF at f_3-f_B was monitored for three typical RH levels (i.e., 40%, 60%, and 80%) for 60 min at a temperature of 25°C. It was obvious that there was only a small frequency fluctuation within 60 min. Hence, this fiber-optic RH sensor exhibited good stability. In order to obtain the response time of the proposed RH sensor, a human breathing experiment was performed directly on the sample (i.e., the GDF device). The ambient RH of the GDF could quickly jump from 28.2% (i.e., room humidity) to 36.4% and then quickly decrease to 28.2%. It is noted that the carbon dioxide

Optics EXPRESS

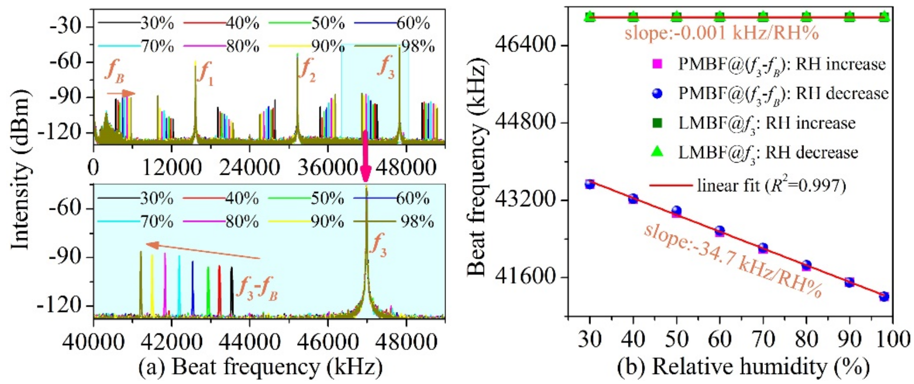

Fig. 6. (a) Beat signals of the fiber laser at different RH levels. (b) Beat signals (i.e., f_3 and f_3-f_B) versus the RH values.

Table 1. Performance of different types of fiber-optic RH sensor based on graphene oxide

Structure	RH range	Sensitivity	Response
Michelson [11]	40%-75%	2.72 nm/%RH	3.6 s
D-shaped fiber [20]	32%-85%	0.15 nm/%RH	66.7 s
	85%-97.6%	0.92 nm/%RH	
micro-knot resonator [18]	0%-80%	0.01 nm/%RH	N/A
core-offset MZI [12]	30-60%	0.03 nm/%RH	N/A
few-mode MZI [19]	30%-55%	~0.19 nm/%RH	N/A
	55%-95%	0.06 nm/%RH	
TFBG [5]	10%-80%	~0.13 dB/%RH	1 s
micro-nano FBG [4]	20%-80%	~0.02 nm/%RH	3.2 s
fiber-tip FP [13]	12.4%-88.4%	0.2 nm/%RH	60 ms
this work	**30%-98%**	**34.7 kHz/%RH**	**64.2 ms**

amount absorbed by the GO at normal temperature and pressure is very small [42]. Hence, the carbon dioxide exhaled by the human body has no effect on response time error of fiber-optic RH sensor. In this experiment, a time-dependent light intensity response was used to monitor the RH variation when a person blows repeatedly into the RH sensor. As shown in Fig. 7(b), the fiber-optic RH exhibited high reversibility, and the average response time and the recovery time for the GDF device were 64.2 ms and 97.8 ms from 10% to 90% of the target RH value, which were faster than those for most of the fiber-optic RH sensors, as shown in Table 1 bellow.

4.5. Temperature measurement of the fiber-optic RH sensor

Moreover, the temperature cross-sensitivity of the RH sensor also needed to be analyzed. As shown in Fig. 8(a), when the temperature was increased from 30°C to 90°C with a step of 10°C, the dominant LMBFs f_N ($N = 1, 2, 3\ldots$) were also mostly unchanged with a constant RH of 50%. Furthermore, the PMBF (i.e., $f_N \pm f_B$) had a small shift with a temperature sensitivity of 4.2 kHz/°C, as shown in Fig. 8(b). It was concluded that the proposed RH sensor exhibited a very low temperature cross sensitivity of 0.12 RH%/°C.

Optics EXPRESS

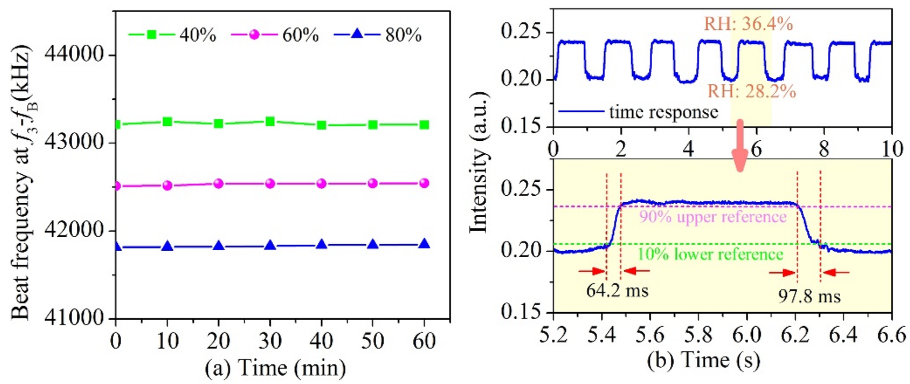

Fig. 7. Stability test of the fiber-optic RH sensor at three RH levels. (b) The response time of the RH sensor.

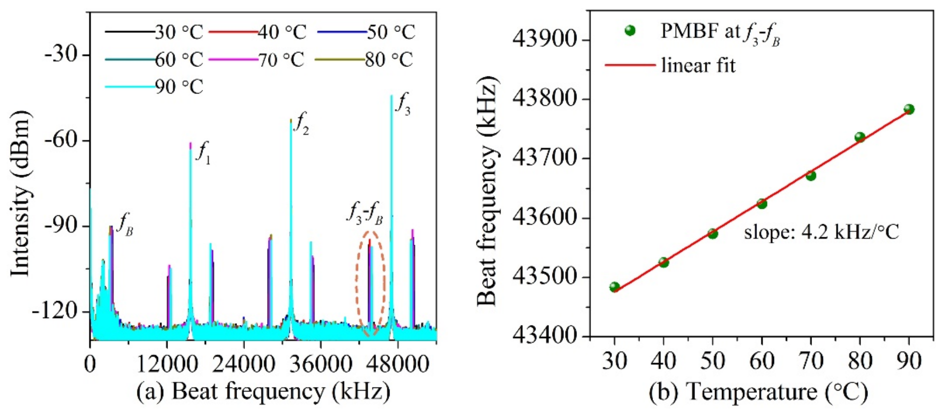

Fig. 8. (a) Temperature response of the fiber-optic RH sensor. (b) Data and a linear fit of the PMBF (i.e., f_3-f_B) versus temperature.

5. Conclusion

In this work, we proposed and demonstrated a fiber laser system for RH sensing based on the beat frequency demodulation. The RH sensor probe was fabricated with GDF, and fiber birefringence of the GDF could be changed for different RH levels. The experimental results showed that the LMBF of the fiber laser had no response to the ambient humidity, and the PMBF of the fiber laser was very sensitive to the various RH levels. It was found that there is a good linear relationship between the PMBF and RH changes in the range of 30% to 98%. The proposed RH sensor exhibits a sensitivity of 34.7 kHz/RH% with a high quality of fit (R^2>0.997). Moreover, the average response and recovery times were measured to be about 64.2 ms and 97.8 ms, respectively. The sensor had the advantages of long stability, reversibility, a quick response, and a low temperature cross-sensitivity. With such highly beneficial properties, the sensor could be used in widespread potential fields, such as biology, chemical processing, and food processing, etc.

Funding. National Natural Science Foundation of China (U1913212, 61875128, 62005170); Guangdong Science and Technology Department (2019TQ05X113, 2021A1515110167, 2021A1515110320); Shenzhen Science and Technology Innovation Program (RCYX20200714114538160, JCYJ20200109114201731, JCYJ20210324100008024).

Disclosures. The authors declare no conflicts of interest.

Optics EXPRESS

Data availability. Data underlying the results presented in this paper are not publicly available at this time but may be obtained from the authors upon reasonable request.

References

1. Z. Chen and C. Lu, "Humidity sensors: A review of materials and mechanisms," Sens. Lett. **3**(4), 274–295 (2005).
2. S. Sikarwar and B. C. Yadav, "Opto-electronic humidity sensor: A review," Sens. Actuators, A **233**, 54–70 (2015).
3. W. Bai, M. H. Yang, J. X. Dai, H. H. Yu, G. P. Wang, and C. J. Qi, "Novel polyimide coated fiber Bragg grating sensing network for relative humidity measurements," Opt. Express **24**(4), 3230–3237 (2016).
4. M. Tian, Y. Huang, C. Li, and M. Lv, "High-performance humidity sensor based on a micro-nano fiber Bragg grating coated with graphene oxide," Opt. Express **28**(18), 26395–26406 (2020).
5. Y. Q. Wang, C. Y. Shen, W. M. Lou, F. Y. Shentu, C. Zhong, X. Y. Dong, and L. M. Tong, "Fiber optic relative humidity sensor based on the tilted fiber Bragg grating coated with graphene oxide," Appl. Phys. Lett. **109**(3), 1–5 (2016).
6. H. Y. Chen, Z. T. Gu, and K. Gao, "Humidity sensor based on cascaded chirped long-period fiber gratings coated with TiO2/SnO2 composite films," Sens. Actuators, B **196**, 18–22 (2014).
7. J. S. Santos, I. M. Raimundo, C. M. B. Cordeiro, C. R. Biazoli, C. A. J. Gouveia, and P. A. S. Jorge, "Characterisation of a Nafion film by optical fibre Fabry-Perot interferometry for humidity sensing," Sens. Actuators, B **196**, 99–105 (2014).
8. Y. Q. Wang, C. Y. Shen, W. M. Lou, and F. Y. Shentu, "Polarization-dependent humidity sensor based on an in-fiber Mach-Zehnder interferometer coated with graphene oxide," Sens. Actuators, B **234**, 503–509 (2016).
9. P. B. Hu, X. Y. Dong, K. Ni, L. H. Chen, W. C. Wong, and C. C. Chan, "Sensitivity-enhanced Michelson interferometric humidity sensor with waist-enlarged fiber bitaper," Sens. Actuators, B **194**, 180–184 (2014).
10. L. P. Sun, J. Li, L. Jin, Y. Ran, and B. O. Guan, "High-birefringence microfiber Sagnac interferometer based humidity sensor," Sens. Actuators, B **231**, 696–700 (2016).
11. R. Chu, C. Y. Guan, Y. T. Bo, J. H. Shi, Z. Zhu, P. Li, J. Yang, and L. B. Yuan, "All-optical graphene-oxide humidity sensor based on a side-polished symmetrical twin-core fiber Michelson interferometer," Sens. Actuators, B **284**, 623–627 (2019).
12. S. Liu, H. Meng, S. Deng, Z. Wei, F. Wang, and C. Tan, "Fiber Humidity Sensor Based on a Graphene-Coated Core-Offset Mach-Zehnder Interferometer," IEEE Sens. Lett. **2**(3), 1–4 (2018).
13. C. Li, X. Yu, W. Zhou, Y. Cui, J. Liu, and S. Fan, "Ultrafast miniature fiber-tip Fabry-Perot humidity sensor with thin graphene oxide diaphragm," Opt. Lett. **43**(19), 4719–4722 (2018).
14. Y. A. D. D. Le and G. Han, "Relative Humidity Sensor Based on a Few-Mode Microfiber Knot Resonator by Mitigating the Group Index Difference of a Few-Mode Microfiber," J. Lightwave Technol. **36**(4), 904–909 (2018).
15. Y. Zhao, R. J. Tong, M. Q. Chen, and F. Xia, "Relative humidity sensor based on hollow core fiber filled with GQDs-PVA," Sens. Actuators, B **284**, 96–102 (2019).
16. L. Xia, L. C. Li, W. Li, T. Kou, and D. M. Liu, "Novel optical fiber humidity sensor based on a no-core fiber structure," Sens. Actuators, A **190**, 1–5 (2013).
17. S. Muto, O. Suzuki, T. Amano, and M. Morisawa, "A plastic optical fibre sensor for real-time humidity monitoring," Meas. Sci. Technol. **14**(6), 746–750 (2003).
18. S. R. Azzuhri, I. S. Amiri, A. S. Zulkhairi, M. A. M. Salim, M. Z. A. Razak, M. F. Khyasudeen, H. Ahmad, R. Zakaria, and P. Yupapin, "Application of graphene oxide based Microfiber-Knot resonator for relative humidity sensing," Results Phys. **9**, 1572–1577 (2018).
19. X. Fan, Q. Wang, M. Zhou, F. Liu, H. Shen, Z. Wei, F. Wang, C. Tan, and H. Meng, "Humidity sensor based on a graphene oxide-coated few-mode fiber Mach-Zehnder interferometer," Opt. Express **28**(17), 24682–24692 (2020).
20. Y. Huang, W. Zhu, Z. Li, G. Chen, L. Chen, J. Zhou, H. Lin, J. Guan, W. Fang, X. Liu, H. Dong, J. Tang, H. Guan, H. Lu, Y. Xiao, J. Zhang, H. Wang, Z. Chen, and J. Yu, "High-performance fibre-optic humidity sensor based on a side-polished fibre wavelength selectively coupled with graphene oxide film," Sens. Actuators, B **255**, 57–69 (2018).
21. R. Gao, Y. Jiang, and W. H. Ding, "Agarose gel filled temperature-insensitive photonic crystal fibers humidity sensor based on the tunable coupling ratio," Sens. Actuators, B **195**, 313–319 (2014).
22. L. H. Chen, T. Li, C. C. Chan, R. Menon, P. Balamurali, M. Shaillender, B. Neu, X. M. Ang, P. Zu, W. C. Wong, and K. C. Leong, "Chitosan based fiber-optic Fabry-Perot humidity sensor," Sens. Actuators, B **169**, 167–172 (2012).
23. J. Ascorbe, J. M. Corres, I. R. Matias, and F. J. Arregui, "High sensitivity humidity sensor based on cladding-etched optical fiber and lossy mode resonances," Sens. Actuators, B **233**, 7–16 (2016).
24. N. Irawati, H. A. Rahman, M. Yasin, S. Al-Askari, B. A. Hamida, H. Ahmad, and S. W. Harun, "Relative Humidity Sensing Using a PMMA Doped Agarose Gel Microfiber," J. Lightwave Technol. **35**(18), 3940–3944 (2017).
25. A. K. Mallik, D. J. Liu, V. Kavungal, Q. Wu, G. Farrell, and Y. Semenova, "Agarose coated spherical micro resonator for humidity measurements," Opt. Express **24**(19), 21216–21227 (2016).
26. D. Su, X. G. Qiao, Q. Z. Rong, H. Sun, J. Zhang, Z. Y. Bai, Y. Y. Du, D. Y. Feng, Y. P. Wang, M. L. Hu, and Z. Y. Feng, "A fiber Fabry-Perot interferometer based on a PVA coating for humidity measurement," Opt. Commun. **311**, 107–110 (2013).
27. Y. H. Luo, C. Y. Chen, K. Xia, S. H. Peng, H. Y. Guan, J. Y. Tang, H. U. Lu, J. H. Yu, J. Zhang, Y. Xiao, and Z. Chen, "Tungsten disulfide (WS2) based all-fiber-optic humidity sensor," Opt. Express **24**(8), 8956–8966 (2016).

Optics EXPRESS

28. B. C. Yao, Y. Wu, A. Q. Zhang, Y. J. Rao, Z. G. Wang, Y. Cheng, Y. Gong, W. L. Zhang, Y. F. Chen, and K. S. Chiane, "Graphene enhanced evanescent field in microfiber multimode interferometer for highly sensitive gas sensing," Opt. Express **22**(23), 28154–28162 (2014).
29. B. C. Yao, C. B. Yu, Y. Wu, S. W. Huang, H. Wu, Y. Gong, Y. F. Chen, Y. R. Li, C. W. Wong, X. D. Fan, and Y. J. Rao, "Graphene-Enhanced Brillouin Optomechanical Microresonator for Ultrasensitive Gas Detection," Nano Lett. **17**(8), 4996–5002 (2017).
30. N. An, T. Tan, Z. Peng, C. Y. Qin, Z. Y. Yuan, L. Bi, C. R. Liao, Y. P. Wang, Y. J. Rao, G. Soavi, and B. C. Yao, "Electrically Tunable Four-Wave-Mixing in Graphene Heterogeneous Fiber for Individual Gas Molecule Detection," Nano Lett. **20**(9), 6473–6480 (2020).
31. Y. H. Guo, N. An, K. K. Guo, Y. W. Li, Y. P. Liang, C. H. Wu, Y. C. Wang, J. He, Y. P. Wang, T. Tan, Y. J. Rao, and B. C. Yao, "Gas detection in a graphene based dual-mode fiber laser microcavity," Sens. Actuators, B **348**, 1–8 (2021).
32. Y. W. Zhu, S. Murali, W. W. Cai, X. S. Li, J. W. Suk, J. R. Potts, and R. S. Ruoff, "Graphene and Graphene Oxide: Synthesis, Properties, and Applications," Adv. Mater. **22**(35), 3906–3924 (2010).
33. D. R. Dreyer, S. Park, C. W. Bielawski, and R. S. Ruoff, "The chemistry of graphene oxide," Chem. Soc. Rev. **39**(1), 228–240 (2010).
34. B. O. Guan, L. Jin, Y. Zhang, and H. Y. Tam, "Polarimetric Heterodyning Fiber Grating Laser Sensors," J. Lightwave Technol. **30**(8), 1097–1112 (2012).
35. L. Gao, L. Chen, L. Huang, and X. Chen, "Multimode fiber laser for simultaneous measurement of strain and temperature based on beat frequency demodulation," Opt. Express **20**(20), 22517–22522 (2012).
36. J. T. Kringlebotn, W. H. Loh, and R. I. Laming, "Polarimetric Er^{3+}-doped fiber distributed-feedback laser sensor for differential pressure and force measurements," Opt. Lett. **21**(22), 1869–1871 (1996).
37. K. K. Guo, J. He, G. X. Xu, and Y. P. Wang, "Dual-Polarization Distributed Feedback Fiber Laser Sensor Based on Femtosecond Laser-Inscribed In-Fiber Stressors for Simultaneous Strain and Temperature Measurements," IEEE Access **8**, 97823–97829 (2020).
38. T. Tan, Z. Y. Yuan, H. Zhang, G. F. Yan, S. Y. Zhou, N. An, B. Peng, G. Soavi, Y. J. Rao, and B. C. Yao, "Multispecies and individual gas molecule detection using Stokes solitons in a graphene over-modal microresonator," Nat. Commun. **12**(1), 1–8 (2021).
39. X. J. Yu, X. F. Chen, J. T. Zhang, Y. C. Gao, and S. C. Liu, "Fiber Birefringence Measurement of Single-Mode Fiber by a Polarimetric Fiber Ring Laser," J. Lightwave Technol. **36**(11), 2204–2210 (2018).
40. X. J. Yu, X. Dong, X. F. Chen, J. T. Zhang, and S. C. Liu, "Polarimetric Multilongitudinal Mode Fiber Laser for Simultaneous Measurement of Strain and Temperature," J. Lightwave Technol. **34**(21), 4941–4947 (2016).
41. K. K. Guo, J. He, S. Q. Cao, M. X. Hou, Z. Zhang, G. X. Xu, and Y. P. Wang, "Beat frequency tuning in dual-polarization distributed feedback fiber laser using side polishing technique," Opt. Express **26**(26), 34699–34710 (2018).
42. S. Chowdhury, G. K. Parshetti, and R. Balasubramanian, "Post-combustion CO2 capture using mesoporous TiO2/graphene oxide nanocomposites," Chem. Eng. J. **263**, 374–384 (2015).